SSRG International Journal of Thermal Engineering
ISSN: 2395-0250/ https://doi.org/10.14445/23950250/IJTE-V11I3P102

Volume 11 Issue 3, 9-29, Sep-Dec 2025

Original Article

Combined effects of Wall Transpiration and Heat Generation/Absorption in a Reactive MHD Casson Nanofluid Past a Cylinder in an Anisotropic Porous Medium

Falomo Bukola Oluwatosin[1], Fenuga Olugbenga John[2], Abiala Israel Olutunji[3]

1,2,3Department of Mathematics, Faculty of Physical and Earth Sciences, University of Lagos, Lagos.

[1]Corresponding Author : bukfalomo@gmail.com

Received: 19 October 2025 Revised: 18 November 2025 Accepted: 17 December 2025 Published: 31 December 2025

Abstract *- This work examines the combined effects of wall transpiration and heat generation/absorption on the unsteady Magnetohydrodynamic Flow of a chemically reactive Casson nanofluid over a cylinder embedded in an anisotropic porous medium. The model incorporates thermal radiation, Joule heating, Brownian motion, thermophoretic diffusion, higher-order chemical reactions, and an induced magnetic field, making the model relevant to applications such as porous resistors and thermal processes in food processing silos. Using similarity transformations, the governing nonlinear partial differential equations are reduced to ordinary differential equations and solved analytically with the Homotopy Perturbation Method (HPM). The results indicate that increasing the Casson parameter (β) and the Slip Parameter ζ enhances flow velocity and decreases temperature due to weakened viscous resistance. Higher radiation parameter Rd and positive heat generation intensify the thermal field. Suction promotes cooling and mass transfer, while injection exhibits an opposite influence. Moreover, a larger Darcy Number (Da), Anisotropic Permeability (Γ), and curvature strengthen convective transport and thermal regulation. Magnetic Parameters (Q, Λ, At) affect field intensity and transient flow behaviour. Overall, the study demonstrates that the interplay between wall transpiration and heat generation/absorption provides effective control over flow structure and thermal performance, offering valuable insights for optimizing industrial thermal-fluid operations and MHD-based energy systems.*

Keywords *- Heat Generation, Anisotropic Porous Medium, Nanofluid, Magnetohydrodynamic.*

1. Introduction

Heat generation and absorption mechanisms are central to the thermal behaviour and operational efficiency of a wide range of engineering, biomedical, and industrial systems. Internal heat sources and sinks arise naturally from physical and chemical processes such as nuclear reactions, electrical dissipation, viscous heating, chemical kinetics, and metabolic activity in biological systems.

In practical applications including nuclear reactors, food processing units, heat exchangers, energy conversion devices, electronic cooling technologies, and biomedical equipment, the regulation of internally generated or absorbed heat is critical for maintaining thermal stability and preventing performance degradation [1,2]. The presence of volumetric heat sources or sinks significantly modifies temperature distributions, thermal boundary-layer thickness, and overall transport characteristics, thereby exerting a pronounced influence on system reliability and thermal efficiency.

From a transport phenomenon perspective, internal heat generation elevates the thermal energy of the fluid, intensifying temperature gradients and buoyancy-driven flow, whereas heat absorption acts as a thermal sink, suppressing temperature rise and stabilizing the thermal field. These mechanisms strongly affect not only the energy equation but also momentum and mass transport through thermo-physical coupling [3]. Consequently, accurate modelling of heat generation and absorption has become indispensable in the analysis and optimization of advanced thermal-fluid systems, particularly those involving reactive flows, high heat fluxes, and energy management technologies.

In recent years, improvements in heat transfer performance have been closely associated with the development of advanced working fluids. One of the most significant developments in this area is the emergence of nanofluids, which are engineered by dispersing nanoscale solid particles into conventional base fluids such as water,

oil, ethylene glycol, or paraffin. The introduction of nanoparticles has been shown to markedly improve thermal conductivity and convective heat transfer performance [4]. Commonly used nanoparticles include aluminium oxide, copper, zinc oxide, titanium dioxide, and carbon-based materials, each contributing distinct thermo-physical characteristics that enhance thermal transport in fluid systems [5].

A widely accepted theoretical framework for nanofluid transport identifies Brownian motion and thermophoresis as the primary mechanisms governing nanoparticle migration relative to the base fluid [6]. These mechanisms become particularly significant in the presence of internal heat generation or absorption, as temperature gradients directly influence nanoparticle diffusion and concentration boundary layers. As a result, the coupled interaction between thermal fields and nanoparticle transport is crucial in determining the overall heat and mass transfer characteristics in nanofluid flows.

Boundary-layer flow over moving and deformable surfaces has long been recognized as a cornerstone problem in fluid mechanics and heat transfer. Classical boundary-layer theory and similarity solutions laid the foundation for understanding flow behaviour over stationary and moving surfaces [7-8]. Subsequent extensions to stagnation-point flows, continuously moving plates, and stretching surfaces established a robust framework for analyzing transport phenomena in diverse industrial processes such as polymer extrusion, coating flows, wire drawing, and continuous casting [9–11]. As industrial systems continue to increase in complexity, the need for more refined fluid models and multiphysical descriptions has become increasingly evident.

In this context, non-Newtonian fluid models have gained prominence for their ability to model materials whose rheological behaviour deviates from Newtonian assumptions. Yield-stress models, in particular, have been shown to provide a more realistic description of fluids such as blood, polymeric solutions, printing inks, and industrial slurries [12–14]. Among these models, the Casson fluid formulation captures the presence of a finite yield stress, resulting in nonlinear momentum transport. When nanoparticles are dispersed within such fluids, the resulting Casson nanofluid exhibits intricate interactions between rheology, thermal transport, and mass diffusion.

The application of magnetic fields to electrically conducting fluids introduces Magnetohydrodynamic (MHD) effects, which offer an effective means of regulating flow behaviour and thermal transport. MHD phenomena are encountered in numerous applications, including nuclear reactor cooling, electromagnetic pumps, metallurgical processing, power generation systems, and biomedical technologies [15-16]. The imposed magnetic field generates Lorentz forces that resist fluid motion, thereby modifying velocity distributions and influencing heat and mass transfer rates. In nanofluid systems, particularly those involving conductive or magnetic nanoparticles, the interaction between magnetic forces and nanoparticle transport further enriches the underlying physics.

A substantial body of literature has examined MHD nanofluid flows under various physical conditions, including mixed convection, thermal radiation, chemical reactions, Joule heating, and entropy generation [17–21]. Despite these advances, many existing studies adopt simplifying assumptions such as isotropic porous media, steady heat source terms, or idealised geometries. Such assumptions restrict the applicability of the results to realistic engineering configurations, where material anisotropy, unsteady thermal effects, and complex boundary conditions are often unavoidable.

Porous media are integral components of many thermal-fluid systems, including packed-bed reactors, geothermal reservoirs, insulation materials, and biological tissues. In practical situations, porous structures often exhibit anisotropy due to material heterogeneity or directional manufacturing processes, leading to variations in permeability along different spatial directions [3]. Anisotropic porous resistance significantly alters momentum and heat transfer behaviour, yet its combined influence with non-Newtonian nanofluids and magnetic fields remains insufficiently explored. Furthermore, wall transpiration via suction or injection is commonly used as a flow-control strategy to regulate boundary-layer thickness, enhance heat transfer, and delay flow separation.

Against this backdrop, a notable gap exists in the literature concerning the simultaneous effects of anisotropic porous media, wall transpiration, unsteady internal heat generation or absorption, and magnetohydrodynamic forces in Casson nanofluid flow. Existing investigations typically address these factors in isolation or under restrictive assumptions, thereby overlooking critical multiphysical interactions. In particular, the combined effects of anisotropic porous resistance and induced magnetic fields on reactive Casson nanofluid flow over cylindrical surfaces have received little attention.

The present study addresses this gap by developing a comprehensive mathematical framework that captures the coupled effects of anisotropic porous media, wall transpiration, unsteady heat generation or absorption, chemical reaction, and magnetic induction in Casson nanofluid flow. By means of similarity transformations, the governing boundary-layer equations are reduced to a system of nonlinear ordinary differential equations, which are solved analytically using the Homotopy Perturbation Method [22]. A detailed parametric investigation is conducted to assess the

influence of governing parameters on the distributions of velocity, temperature, concentration, and the magnetic field. Engineering quantities of practical relevance, including skin friction coefficient, Nusselt number, and Sherwood number, are evaluated to quantify drag force, heat transfer rate, and mass transfer rate. The findings provide new insight into coupled transport mechanisms and establish guidelines for the design and optimization of MHD-based thermal-fluid systems.

2. Formulation of the Problem

This section is premised on the physical concept of problem modelling leading to governing Partial Differential Equations (PEDs) and the selected appropriate boundary conditions concerning the Casson viscoelastic nanofluid flow, heat, and mass transfer past the cylindrical surface of two different orientations embedded in an anisotropic porous medium in the presence of an induced magnetic field.

Figure 1 depicts schematics of two-dimensional, incompressible, laminar, inclined solid and hollow cylinders, immersed in a Casson electrically and thermally conducting nanofluid in the presence of a higher-order chemical reaction and an induced magnetic field. Thermal radiation, higher-order heat sources or sinks, Joule heating, and thermal energy dissipation are all considered.

The formulations are based on the assumptions that the axial axis (z) is perpendicular to the radial axis (r), and that the fluid and porous medium are in perpetual thermal equilibrium with no surface slipperiness. All physical properties are constant, except for the porous medium's permeability and the fluid density, which have a linear variation exclusively in the buoyancy term of the momentum equations, adhering to the Oberbeck-Boussinesq approximation. The flow is driven by the combined effect of a linearly stretching cylinder wall and an ambient stream from the stagnation point, both acting in the axial direction with Velocity Uw(z). The nanofluid is maintained below its boiling point everywhere in the flow regime, and the nanoparticles and base fluid are in thermal equilibrium. Furthermore, the influence of magnetic polarization is considered negligible, while the effect of the electric field is significant, and the analysis ignores the effects of Hall current and ion-slip.

By means of extant similarity transformations, PDEs are reduced to ODEs. This study is based on a cylindrical coordinate system with velocity $V = (v = u_r, w = u_\vartheta = 0, u = u_z)$ for two-dimensional or axially symmetric physical models. Any fluid is located at a point (r, ϑ, z) with velocity $v = (u = u_r, w = u_\vartheta, u = u_z)$, and the assumption of two-dimensional flow ensures that $\left(\vartheta, \frac{\partial}{\partial \vartheta}\right) = 0$.

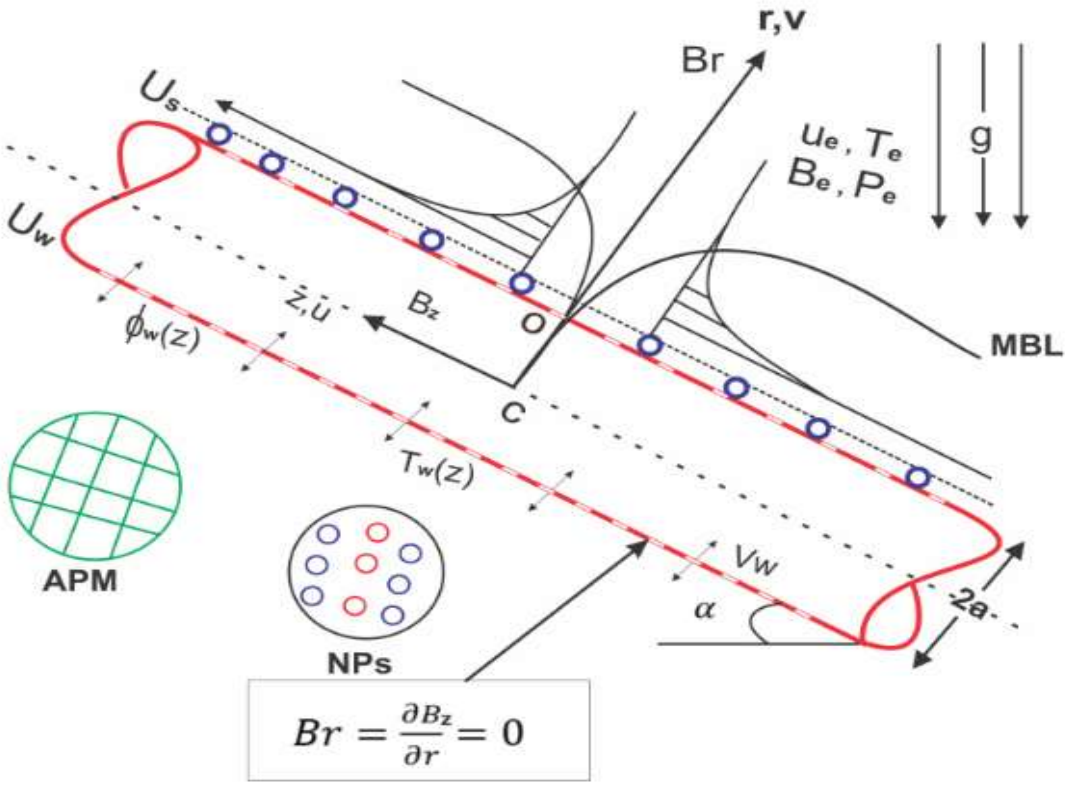

Fig. 1 Practical Flow Simulation Exposition Chart

Continuity and magnetic solenoidal nature equations are then reduced to two-dimensional differential forms:

$$\frac{\partial(rv)}{\partial r}+\frac{\partial(ru)}{\partial z}=0 \tag{1}$$

$$\frac{\partial(rB_r)}{\partial r}+\frac{\partial(rB_z)}{\partial z}=0 \tag{2}$$

Where $B=(B_r,B_\vartheta=0,B_z)$ is the induced magnetic field.

The momentum, energy, and nanoparticle volume fraction are:

$$\frac{\partial u}{\partial t}+\left(u\frac{\partial}{\partial z}+v\frac{\partial}{\partial r}\right)u=\frac{1}{\rho_f}\Big[\quad -\frac{\partial p}{\partial z}+\mu\left(1+\frac{1}{\beta}\right)\nabla^2u+F_z-\frac{\mu}{\rho_f K_2}\Gamma(K^*,\vartheta)\left(1+\frac{1}{\beta}\right)u\Big] \tag{3}$$

where the axial component of the resultant body force is

$$F_z=\left[-(\rho_p-\rho_f)(\phi-\phi_\infty)+(1-\phi_\infty)\rho_f(\beta_T(T-T_\infty))\right]g\,sin(\alpha)+\frac{1}{\mu_m}\left(B_r\frac{\partial B_z}{\partial r}+B_z\frac{\partial B_z}{\partial z}\right)$$

$$(\rho C)_f\left(\frac{\partial}{\partial t}+u\frac{\partial}{\partial z}+v\frac{\partial}{\partial r}\right)T=\left[\begin{array}{c} k_f\nabla^2T-\frac{1}{r}\frac{\partial}{\partial r}(rq_r)+\mu\left(1+\frac{1}{\beta}\right)\left(\frac{\partial u}{\partial r}\right)^2+Q_0(T-T_\infty)^{\varpi} \\ +(\rho C)_p\left\{D_B\nabla\phi\cdot\nabla T+\frac{D_T}{T_\infty}\nabla T\cdot\nabla T\right\}+\frac{1}{\sigma}J^2 \end{array}\right] \tag{4}$$

$$\left(\frac{\partial}{\partial t}+u\frac{\partial}{\partial z}+v\frac{\partial}{\partial r}\right)\phi=D_B\frac{1}{r}\frac{\partial}{\partial r}\left(r\frac{\partial\phi}{\partial r}\right)+\frac{D_T}{T_\infty}\frac{1}{r}\frac{\partial}{\partial r}\left(r\frac{\partial T}{\partial r}\right)-\kappa_r(\phi-\phi_\infty)^m \tag{5}$$

$$\left(\frac{\partial}{\partial t}+u\frac{\partial}{\partial z}+v\frac{\partial}{\partial r}\right)B_z=B_z\frac{\partial u}{\partial z}+B_r\frac{\partial u}{\partial r}+\frac{\eta_m}{r}\frac{\partial}{\partial r}\left(r\frac{\partial B_z}{\partial r}\right) \tag{6}$$

The initial and boundary conditions are Kumar and Seth [36] and Attia et al. [44]

$$\begin{gathered} t\le 0: u=v=0, T=T_\infty, B=(B_e(t,z),0), \phi=\phi_\infty \text{ forall } (r,\vartheta,z)\in\Re^3, \\ \text{where } B_z=B_e(t,z)=B_0\left(\frac{z}{l|1-\lambda t|}\right) \end{gathered} \tag{7}$$

$$t>0:\begin{cases} u=U_w(t,z), v=V_w(t,z), T=T_w(t,z)=T_\infty+\frac{b_1}{|1-\lambda t|}z^n, \\ \phi=\phi_w(t,z)=\phi_\infty+\frac{b_0}{|1-\lambda t|}z^n, B_r=\frac{\partial B_z}{\partial r}=0 \text{ or } r=a \\ u_e(t,z)=U_e\left(\frac{z}{l|1-\lambda t|}\right), \frac{\partial u}{\partial r}\to 0, T\to T_\infty, \\ B_z\to B_e(t,z)=B_0\left(\frac{z}{l|1-\lambda t|}\right), \phi\to\phi_\infty \text{ as } r\to\infty \end{cases} \tag{8}$$

Introducing the following similarity transformations

$$\begin{gathered} \eta=\frac{r^2-a^2}{2a}\sqrt{\frac{U_w}{\nu z}}, u_z\equiv u=U_wf'(\eta), \theta=\frac{T-T_\infty}{T_w-T_\infty}, \varphi=\frac{\varphi-\varphi_\infty}{\varphi_w-\varphi_\infty}, u_r\equiv v=-\frac{a}{r}\sqrt{\frac{\nu U_w}{z}}f(\eta), \\ B_z=B_0\left(\frac{z}{a}\right)h'(\eta), B_r=-\frac{B_0}{r}\sqrt{\frac{\nu z}{U_w}}h(\eta), a\neq 0 \& U_w=U\left(\frac{z}{l|1-\lambda t|}\right) \end{gathered} \tag{9}$$

The similarity transformation given in equation 9 above, derived using Lie group analysis see Adeniyan et al. [45]), satisfies the conservation of mass flow (continuity equation) and the solenoidal nature law of magnetic field. The dimensionless momentum, energy, chemically reactive nanoparticle balance, and the magnetic induction balance equations are derived as

$$\left(1+\frac{1}{\beta}\right)\left[(1+2\gamma\eta)f\left|{}^{\prime\prime\prime}-{}^{\prime\prime 2}(\theta-N_r\varphi)\left(1+\frac{1}{\beta}\right)'\right.+QZ^2\left(h'^2-hh''()^2\right)\right] \tag{10}$$

$$\frac{1}{Pr}(1+R_d)\left\{(1+2\gamma\eta)\theta^{'''}\{\}\left(1+\frac{1}{\beta}\right)^{'2''} 0G\theta^{\varpi}+(1+2\gamma\eta)\{N_b\varphi^{'}\theta^{'}+N_t\theta^{'2}\}+Q\Lambda Ech^{'2}\right\} \tag{11}$$

$$\frac{1}{Sc}\left\{(1+2\gamma\eta)\varphi^{'''}\{\}^{''}\frac{1}{LePr}\frac{N_t}{N_b}\left\{(1+2\gamma\eta)\theta^{'''}\{\}^{2^m}\right\}\right\} \tag{12}$$

$$\Lambda\left\{(1+2\gamma\eta)h^{'''}{}^{''t\left(h^{'}+\frac{1}{2}\eta h^{''}(0)\right)}\right\} \tag{13}$$

The boundary conditions are given as

$$f^{'}(0)=1+\zeta\left(1+\frac{1}{\beta}\right)f$$

$$f^{'}{}_{w}{}^{\text{at}}f^{'}(\eta)=\Omega,h^{'}(\eta)=1,\theta(\eta)=\varphi(\eta)=0 \quad \text{as} \quad \eta\to\infty \tag{14}$$

Where $N_r=\frac{(\rho_p-\rho_f)}{\rho_f(1-\phi_\infty)\beta_T(T_w-T_\infty)}$ is the bouyancy ratio,$Ri=(1-\phi_\infty)\beta_T(T_w-T_\infty)\frac{gz}{U_w^2}$ is the modified local Ricardson number, $A=\frac{l\lambda}{U}$ is the transient (unsteadiness) parameter, $A_t=\frac{\lambda a}{U|1-\lambda t|}$ is the local transient (unsteadiness) parameter with the constant $l=a$, $Q=\frac{B_0^2}{\rho\mu_m U^2}$ is the Chandrasekhar number, $\Lambda=\frac{(1-\lambda t)\mu_m}{lU}$ is the local inverse modified magnetic Prandtl number, $\gamma=\frac{1}{a}\sqrt{\frac{\nu z}{U_w}}$ is the curvature parameter, $Ec=\frac{U_w^2}{C_f\Delta T}$ is the Eckert number, $Pr=\frac{\nu}{\alpha_f}$ is the (Thermal) Prandtl number, α_f is the thermal diffusivity, $R_d=\frac{16\sigma^*}{3k_fk^*}T_\infty^3$ is the Rosseland radiation parameter, $N_b=\tau_0\frac{D_B\Delta\phi}{\nu}, N_t=\tau_0\frac{D_T\Delta T}{\nu T_\infty}$ are the Brownian and thermophoretic parameters, $Le=\frac{\alpha_f}{D_B}$ is the modified Lewis number, $\kappa^2=\frac{z\kappa_r}{U_w}(\Delta\phi)^{m-1}$ is the chemical reaction parameter of the nanofluid, $\zeta=N\sqrt{\frac{U_w}{\nu U_w}}$ is the slip parameter, $f_w=V_w\sqrt{\frac{z}{\nu U_w}}$ is the surface mass flux (suction/injection) at the wall surface. $\Omega=\frac{U_e}{U}$ Is the velocity ratio of the free stream.

2.1. Parameters of Engineering Interest

The three main physical quantities are the local Nusselt number Nu_z, the local Sherwood number NSh_z , and the local skin friction coefficient C_f.

$$C_f=\frac{\tau_w}{\rho_f U_w^2}, Nu_z=\frac{zq_w}{k_f\Delta T}, \text{and } NSh_z=\frac{zj_w}{D_B\Delta\phi} \tag{15}$$

where j_w the model of the nanofluid volume fraction (flux) transfer at the cylinder wall τ_w is the skin friction/shear stress along the stretching surface, and q_w the wall heat flux is considered, considering the effect of thermal radiation.

$$\begin{cases}\tau_w=\mu\left(1+\frac{1}{\beta}\right)\left(\frac{\partial u}{\partial r}\right)_{r=0}\\ q_w=\frac{z}{\Delta T}k_f\left(1+\frac{16\sigma^*T_\infty^3}{3k_fk^*}\right)\left(\frac{\partial T}{\partial r}\right)_{r=0}, \text{and}\\ j_w=D_B\left(\frac{\partial\phi}{\partial r}\right)_{r=0}\end{cases} \tag{16}$$

substituting the non-dimensionless parameters

$$\begin{cases} Re_z^{\frac{1}{2}} C_f = (1+\frac{1}{\beta}) f^{'} \\ Re_z^{-\frac{1}{2}} Nu_z = (1+R_d)\theta^{'}(0) \\ Re_z^{-\frac{1}{2}} NSh_z = \vartheta^{'}(0) \end{cases} \tag{17}$$

where $Re_z = \frac{U_w z}{\nu}$ is the local Reynolds number.

3. Method of Solution

3.1. Homotopy Perturbation Method

He [47], He [48], and He [49] upgraded the homotopy perturbation method that originally He [46] had introduced as a general analytical power series approach for solving nonlinear equations. The underlying concept of this approach is briefly summarized in this section.

$$A(U) - g(\sigma) = 0, \sigma \in \Delta \tag{1}$$

in accordance with the prescribed boundary conditions

$$B\left(u, \frac{\partial u}{\partial \sigma}\right) = 0, \sigma \in \Gamma \tag{2}$$

Where $g(\sigma)$ is a known analytical function, B is a boundary operator, A is a general differential operator, and Γ is the domain Δ boundary. L and N, which stand for linear and nonlinear operators, respectively, are the two components of the operator A. As a result, equation (18) can be rewritten as follows.

$$L(u) + N(u) - g(\sigma) = 0 \tag{3}$$

A homotopy $U(\sigma, p)$: $\Delta \times [0,1] \rightarrow R$ that satisfies the equation can be created using the homotopy technique.

$$\mathcal{H}(U,p) = (1-p)[L(u) - L(u_0)] + p[A(u) - g(\sigma)] = 0, p \in [0,1], \tag{4}$$

or the equation

$$\mathcal{H}(U,p) = L(U) - L(U_0) + pL(U_0) + p[N(u) - g(\sigma)] = 0 \tag{5}$$

U_0 It is an initial approximation of U in (26) that should meet the boundary conditions and $p \in [0,1]$ is an embedding parameter in equations (21) and (22). Subsequently, equations (21) and (22) lead to:

$$\mathcal{H}(U,0) = L(U) - L(U_0) = 0, \tag{6}$$

$$\mathcal{H}(U,0) = A(U) - g(\sigma) = 0. \tag{7}$$

Just as $U(\sigma, p)$ changes from $U_0(\sigma)$ to $U(\sigma)$ p changes from zero to unity. The term homotopy in topology refers to this. Equation (25) illustrates how the solution of equations (21) and (22) can be expressed as a power series in p when the embedding parameter is small.

$$U = U_0 + pU_1 + p^2 U_2 + \cdots \tag{8}$$

It should be noted that p_{it} has values between 0and1 with $p = 1$ yielding the best outcome. Consequently, the approximate solution to equation (18) is obtained by setting $p = 1$:

$$u = \lim_{p \to 1} U = U_0 + U_1 + U_2 + \ldots \tag{9}$$

Combining the Homotopy and Perturbation Methods is the fundamental concept mentioned above. In order to get around the drawbacks of the conventional perturbation methods, the technique is known as the Homotopy Perturbation Method (HPM). However, this method can offer every benefit of the conventional perturbation methods. In the majority of cases, the series in equation (26) is convergent.

3.2. Application of HPM to the Problem

The HPM is applied to the equations (10)-(13) as

$$\mathscr{H}_f(\eta,f,\theta,\varphi,h,p) \equiv (1-p)\left(1+\frac{1}{\beta}\right)f$$

$$+p\left[\left(1+\frac{1}{\beta}\right)\left[(1+2\gamma\eta)f\right]-\Gamma Da\left(1+\frac{1}{\beta}\right)(f'-\Omega)+QZ^2\left(h^2-hh''(0)^2\right)=0\right] \tag{10}$$

$$\mathscr{H}_\theta(\eta,f,\theta,\varphi,h,p) \equiv (1-p)\frac{(1+R_d)}{Pr}\theta''$$

$$+p\left[\frac{(1+R_d)}{Pr}\left\{(1+2\gamma\eta)\theta''\{\}\left(1+\frac{1}{\beta}\right)^{2}\right\}+f\theta'-nf'\theta+G\theta^{\varpi}+(1+2\gamma\eta)\{N_b\varphi'\theta'+N_t\theta'^2\}+Q\Lambda Ech^{2}\right\}=0\right] \tag{11}$$

$$\mathbb{H}_\varphi(\eta,f,\theta,\varphi,h,p) \equiv (1-p)\frac{1}{Sc}\varphi''\left[\begin{array}{c}\frac{1}{Sc}\left\{(1+2\gamma\eta)\varphi''\{\}''\right\}\\ +\frac{1}{LePrN_b}\left\{(1+2\gamma\eta)\theta''\{\}^2m\right\}\end{array}=0\right] \tag{12}$$

$$\mathscr{H}_h(\eta,f,\theta,\varphi,h,p) \equiv (1-p)\Lambda h$$

$$+p\left[\Lambda\left\{(1+2\gamma\eta)h''-t\left(h'+\frac{1}{2}\eta h''(0)\right)\right\}\right] \tag{13}$$

The solutions of the preceding equations may be expressed as a power series in p, as presented in equations (31).

$$\begin{aligned} f &= f_0+pf_1+p^2f_2+p^3f_3+\cdots\\ \theta &= \theta_0+p\theta_1+p^2\theta_2+p^3\theta_3+\cdots\\ \varphi &= \varphi_0+p\varphi_1+p^2\varphi_2+p^3\varphi_3+\cdots\\ h &= h_0+ph_1+p^2h_2+p^3h_3+\cdots \end{aligned} \tag{14}$$

Substituting equation (31) and its respective derivatives into equations (10)(13) to get

$$\begin{aligned} &(1-p)\left(1+\frac{1}{\beta}\right)(f_0'''+pf_1'''+p^2f_2'''+\ldots)+\\ &p\left[\begin{array}{l}\left(1+\frac{1}{\beta}\right)[(1+2\gamma\eta)(f_0'''+pf_1'''+p^2f_2'''+\ldots)+2\gamma(f_0''+pf_1''+p^2f_2''+\ldots)]\\ +(f_0+pf_1+p^2f_2+\ldots)(f_0''+pf_1''+p^2f_2''+\ldots)-(f_0'+pf_1'+p^2f_2'+\ldots)^2\\ +Ri\left(\theta_0+p\theta_1+p^2\theta_2+\ldots-N_r(\varphi_0+p\varphi_1+p^2\varphi_2+\ldots)\right)+A\Omega-\Omega^2\\ -\Lambda Da\left(1+\frac{1}{\beta}\right)(f_0'+pf_1'+p^2f_2'+\ldots-\Omega)-QZ^2\\ +QZ^2(h_0'+ph_1'+p^2h_2'+\ldots)-(h_0+ph_1+p^2h_2+\ldots)(h_0''+ph_1''+p^2h_2''+\ldots)\end{array}\right]=0 \end{aligned} \tag{15}$$

$$(1-p)\frac{(1+R_d)}{Pr}(\theta_0''+p\theta_1''+p^2\theta_2''+\ldots)+$$
$$p\begin{bmatrix}\frac{(1+R_d)}{Pr}\left[(1+2\gamma\eta)(\theta_0''+p\theta_1''+p^2\theta_2''+\ldots)+2\gamma(\theta_0'+p\theta_1'+p^2\theta_2'+\ldots)\right]\\+Ec\left(1+\frac{1}{\beta}\right)(1+2\gamma\eta)(f_0''+pf_1''+p^2f_2''+\ldots)^2+G(\theta_0+p\theta_1+p^2\theta_2+\ldots)^{\varpi}\\+(f_0+pf_1+p^2f_2+\ldots)(\theta_0'+p\theta_1'+p^2\theta_2')-n(f_0'+pf_1'+p^2f_2'+\ldots)(\theta_0+p\theta_1+p^2\theta_2)\\+(1+2\gamma\eta)\left\{N_b(\varphi_0'+p\varphi_1'+p^2\varphi_2'+\ldots)(\theta_0'+p\theta_1'+p^2\theta_2')+N_t(\theta_0'+p\theta_1'+p^2\theta_2')^2\right\}\\+Q\Lambda Ec(h_0''+ph_1''+p^2h_2''+\ldots)^2\end{bmatrix}=0 \quad (16)$$

$$(1-p)\frac{1}{Sc}(\varphi_0''+p\varphi_1''+p^2\varphi_2''+\ldots)+$$
$$+p\begin{bmatrix}\frac{1}{Sc}[(1+2\gamma\eta)(\varphi_0''+p\varphi_1''+p^2\varphi_2''+\ldots)+2\gamma(\varphi_0'+p\varphi_1'+p^2\varphi_2'+\ldots)]\\+(f_0+pf_1+p^2f_2+\ldots)(\varphi_0'+p\varphi_1'+p^2\varphi_2'+\ldots)-n(f_0'+pf_1'+p^2f_2'+\ldots)\times\\(\varphi_0+p\varphi_1+p^2\varphi_2)\\+\frac{1}{LePr}\frac{N_t}{N_b}[(1+2\gamma\eta)(\theta_0''+p\theta_1''+p^2\theta_2''+\ldots)+2\gamma(\theta_0'+p\theta_1'+p^2\theta_2'+\ldots)]\\-\kappa^2(\varphi_0+p\varphi_1+p^2\varphi_2)^m\end{bmatrix}=0 \quad (17)$$

$$(1-p)\Lambda(h_0'''+ph_1'''+p^2h_2'''+\ldots)$$
$$+p\begin{bmatrix}\Lambda[(1+2\gamma\eta)(h_0'''+ph_1'''+p^2h_2'''+\ldots)+2\gamma(h_0''+ph_1''+p^2h_2''+\ldots)]\\(f_0+pf_1+p^2f_2+\ldots)(h_0''+ph_1''+p^2h_2''+\ldots)-(h_0+ph_1+p^2h_2+\ldots)\\(f_0''+pf_1''+p^2f_2''+\ldots)\\-A_t\left((h_0'+ph_1'+p^2h_2'+\ldots)+\frac{1}{2}\eta(h_0''+ph_1''+p^2h_2''+\ldots)\right)\end{bmatrix}=0 \quad (18)$$

Also, the boundary conditions in the equation (17) result in:

$$f_0(0)+pf_1(0)+p^2f_2(0)+\cdots=-f_w \quad (36a)$$
$$f_0'(0)+pf_1'(0)+p^2f_2'(0)+\cdots=1+\zeta\left(1+\tfrac{1}{\beta}\right)(f''^{\,2}_0+f''^{\,2}_1+f''^{\,2}_2) \quad (36b)$$
$$h_0(0)+ph_1(0)+p^2h_2(0)+\cdots=0 \quad (36c)$$
$$h'^{\,2}_0+h'^{\,2}_1+h'^{\,2}_2 \quad (36d)$$
$$\theta_0(0)+p\theta_1(0)+p^2\theta_2(0)+\cdots=1 \quad (36e)$$

$$\varphi_0(0) + p\varphi_1(0) + p^2\varphi_2(0) + \cdots = 1 \tag{36f}$$

$$f_0^{'}(\infty) + pf_1^{'}(\infty) + p^2 f_2^{'}(\infty) + \cdots = \Omega \tag{36g}$$

$$h_0^{'}(\infty) + ph_1^{'}(\infty) + p^2 h_2^{'}(\infty) + \cdots = 1 \tag{36h}$$

$$\theta_0(\infty) + p\theta_1(\infty) + p^2\theta_2(\infty) + \cdots = 0 \tag{36i}$$

$$\varphi_0(\infty) + p\varphi_1(\infty) + p^2\varphi_2(\infty) + \cdots = 0 \tag{36j}$$

To be able to arrange the equations above and their boundary conditions according to the powers of the embedding parameter p, this study specifies the value(s) of $n(= 0,1,2,3)$ and subsequently obtains:

$$p^{(0)}: \left(1+\tfrac{1}{\beta}\right) f''' = 0, \frac{(1+R_d)}{Pr}\theta \frac{1}{Sc} \text{and}''' = 0_{0_{0''}{}_{0''}{}_0} \text{(37a)} f_0(0) = -f_w, f_{0'}(0) = 1 + \zeta\left(1+\tfrac{1}{\beta}\right) f00_{0_{0'}{}_{0'}{}_{0''}} \text{(37b)} f_{0'}(\infty) = \Omega, h_{0'}(\infty) = 1, \theta_0(\infty) = \varphi_0(\infty) = 0 \tag{37c}$$

$$p^{(1)}: \begin{matrix} \left(1+\frac{1}{\beta}\right) f_{1'''} + 2\gamma\left(1+\frac{1}{\beta}\right)\eta f_{0'''} + 2\gamma\left(1+\frac{1}{\beta}\right) f_{0''} + f_0 f_{0''} - f_{0'}^2 + Ri(\theta_0 - N_r\varphi_0) \\ -\Lambda Da\left(1+\frac{1}{\beta}\right)(f_{0'} - \Omega) + QZ^2(h_{0'}^2 - h_0 h_{0''} - 1) + A\Omega + \Omega^2 \end{matrix} = 0 \text{(38a)} f_1(0) = 0, f_{1'}(0) = \zeta\left(1+\tfrac{1}{\beta}\right) f1'_{1'} \tag{38b}$$

$$\frac{(1+Rd)}{Pr}\theta_{1''} + \frac{2\gamma(1+Rd)}{Pr}\eta\theta_{0''} + \frac{2\gamma(1+Rd)}{Pr}\theta_{0'} + Ec\left(1+\frac{1}{\beta}\right)(1+2\gamma\eta) f_{0''}^2 + f_0\theta_{0'} = 0 \tag{39a}$$

$$-nf_{0'}\theta_0 + G\theta_0 + (1+2\gamma\eta)\left(N_b\varphi_{0'}\theta_{0'} + N_t\theta_{0'}^2\right) + Q\Lambda Ech_{0''}^2$$

$$\theta_1(0) = 0, \theta_1(\infty) = 0 \tag{39b}$$

$$\frac{1}{Sc}\varphi\frac{2\gamma}{Sc}\frac{2\gamma}{Sc}{}_{0'}{}_{0_{0'}}{}_{0'}{}_0 \frac{1}{LePr}\frac{N_t}{N_b}\left\{(1+2\gamma\eta)\theta 0'_{0''}\{\}^2{}_0\right\}_{0''_{1''}} \text{(40a)} \varphi_1(0) = 0, \varphi_1(\infty) = 0 \tag{40b}$$

$$\Lambda h^{'^{'}} + 2\gamma\Lambda\eta h^{'^{'}} + 2\gamma\Lambda h0t\left(h_{0'} + \frac{1}{2}\eta h_{0'}()\right)_{0'_{0'_{0_1}}} \tag{41a}$$

$$h_1(0) = 0, h1'_{1'} \tag{41b}$$

$$p^{(2)}: \begin{matrix} \left(1+\frac{1}{\beta}\right) f_2''' + \left(1+\frac{1}{\beta}\right)\left(2\gamma\eta f_1'' + 2\gamma f_1'\right) + f_0 f_1'' + f_1 f_0'' - 2f_0' f_1' \\ +Ri(\theta_1 - N_r\varphi_1) + QZ^2\left(2h_{0'}h_{1'} - h_0 h_{1''} - h_1 h_{0''}\right) - \Gamma Da\left(1+\frac{1}{\beta}\right) f_{1'} \end{matrix} = 0 \tag{42a}$$

$$f_2(0) = 0, f_{2'}(0) = \zeta\left(1+\tfrac{1}{\beta}\right) f2'_{2'} \tag{42b}$$

$$\begin{matrix} \frac{(1+R_d)}{Pr}\theta_{2''} + \frac{(1+R_d)}{Pr}\left(2\gamma\eta\theta_{1''} + 2\gamma\theta_{1'}\right) + 2Ec\left(1+\frac{1}{\beta}\right)(1+2\gamma\eta) f_{0''} f_{1''} + f_0\theta_{1'} \\ + f_1\theta_{0'} - nf_{0'}\theta_1 - nf_{1'}\theta_0 + G\theta_1 + (1+2\gamma\eta)\left(N_b\varphi_{0'}\theta_{1'} + N_b\varphi_{1'}\theta_{0'} + 2N_t\theta_{0'}\theta_{1'}\right) \\ +2Q\Lambda Ech_{0''}h_{1''} \end{matrix} = 0 \tag{43a}$$

$$\theta_2(0) = 0, \theta_2(\infty) = 0 \tag{43b}$$

$$\frac{1}{Sc}\varphi_{2''} + \frac{1}{Sc}\left(2\gamma\eta\varphi_{1''} + 2\gamma\varphi_{1'}\right) + \frac{1}{PrLe}\frac{N_t}{N_b}\left((1+2\gamma\eta)\theta_{1''} + 2\gamma\theta_{1'}\right) = 0 \tag{44a}$$

$$-\kappa^2\varphi_1 + f_0\varphi_{1'} + f_1\varphi_{0'} - nf_{0'}\varphi_1 - nf_{1'}\varphi_0$$

$$\varphi_2(0) = 0, \varphi_2(\infty) = 0 \tag{44b}$$

$$\Lambda h''' + \Lambda\left(2\gamma\eta h''' + 2\gamma h_{1''}()_0 101t\left(h\frac{1}{2_{1'}}_{1''}\right)_{0''}{}_{1''}{}_{0''}{}_{1''}{}_1\right)_2 \tag{45a}$$

$$h_2(0) = 0, h1'_{2'} \tag{45b}$$

For ease of convergence and less computational power, this research work employs some initial solutions for f_0, θ_0, φ_0, and h_0 as

$$f_0 = a_1 + b_1\eta + c_1\, exp(-k\eta) \tag{46}$$

$$\theta_0 = a_2 + b_2\, exp(-k\eta) \tag{47}$$

$$\varphi_0 = a_3 + b_3\, exp(-k\eta) \tag{48}$$

$$h_0 = a_4 + b_4\eta + c_4\, exp(-k\eta) \tag{49}$$

where a_i, b_i, c_i, and d_i $i = 1,2,3,4$ are arbitrary constants;

Solving the equation (65) conforming to the boundary conditions in the equation 3.2 (3.2) to obtain

$$f_0(\eta) = -f_w + \Omega\eta - \alpha(1 - exp(-k\eta)), \theta_0(\eta) = exp(-k\eta), \varphi_0(\eta\, exp(-k\eta), \text{and } h_0(\eta) = \eta \tag{50}$$

where $\alpha = \frac{\Omega-1}{k\left\{1+\zeta\left(1+\frac{1}{\beta}k\right)\right\}}$

Equations (69) make the solutions easy to compute f_i, θ_i, φ_i, and h_i $i = 1,2, \ldots$ analytically, and solve them with their respective boundary conditions. Therefore, taking the limit as $p \to 1$ for f_i, θ_i, φ_i, and h_i, $i = 0,1,2, \ldots$ and taking the form as in the equation (9) , then

$$f(\eta) = f_0(\eta) + f_1(\eta) + f_2(\eta) + \cdots \tag{51}$$

$$\theta(\eta) = \theta_0(\eta) + \theta_1(\eta) + \theta_2(\eta) + \cdots \tag{52}$$

$$\varphi(\eta) = \varphi_0(\eta) + \varphi_1(\eta) + \varphi_2(\eta) + \cdots \tag{53}$$

$$h(\eta) = h_0(\eta) + h_1(\eta) + h_2(\eta) + \cdots \tag{54}$$

4. Results and Discussion

In this work, the coupled effects of heat generation/absorption and wall transpiration in a reactive MHD Casson Nanofluid past a cylinder in an anisotropic porous medium are examined and resolved using the Homotopy Perturbation Method. A graphical representation of equations (10-14) is provided by HPM for additional analysis of their effects on the velocity, temperature, nanoparticle propagation, and magnetic profiles. The results are calculated using the Maple 2016 solver for the semi-analytic method HPM. The analytical solutions' numerical computation is carried out by giving the parameters a specific value.

$$\beta = 0.3, \varsigma = 0.2, \gamma = 0.5, Q = 0.2, Z = 1, \Omega = 0.1, Ri = 3, Nr = 0.5, Da = 2, Rd = 0.2, Pr = 0.71,$$
$$Ec = 0.1, N_b = 0.01, N_t = 0.03, \Gamma = 1.5, n = 1, Sc = 0.63, Le = 0.63, \kappa = 3, m = 1, A_t = 0.6$$ Except otherwise stated.

Figures 2(a–d) depict the influence of the Casson parameter β on velocity, temperature, nanoparticle concentration, and magnetic field distributions. Increasing β reduces fluid yield stress, transitioning the Casson nanofluid toward Newtonian behavior. Consequently, the axial velocity rises (Figure 2a) while temperature decreases (Figure 2b) due to enhanced momentum diffusion and diminished viscous resistance. The nanoparticle concentration (Figure 2c) also shows thinning of the boundary layer under suction and a slight thickening under injection. Similarly, magnetic field intensity (Figure 2d) weakens with higher β, as less viscous fluids allow easier distortion of field lines. Also, in Figures 13b–15b affecting the skin-friction, Nusselt, and Sherwood numbers, confirming that higher β boosts heat and mass transfer efficiency.

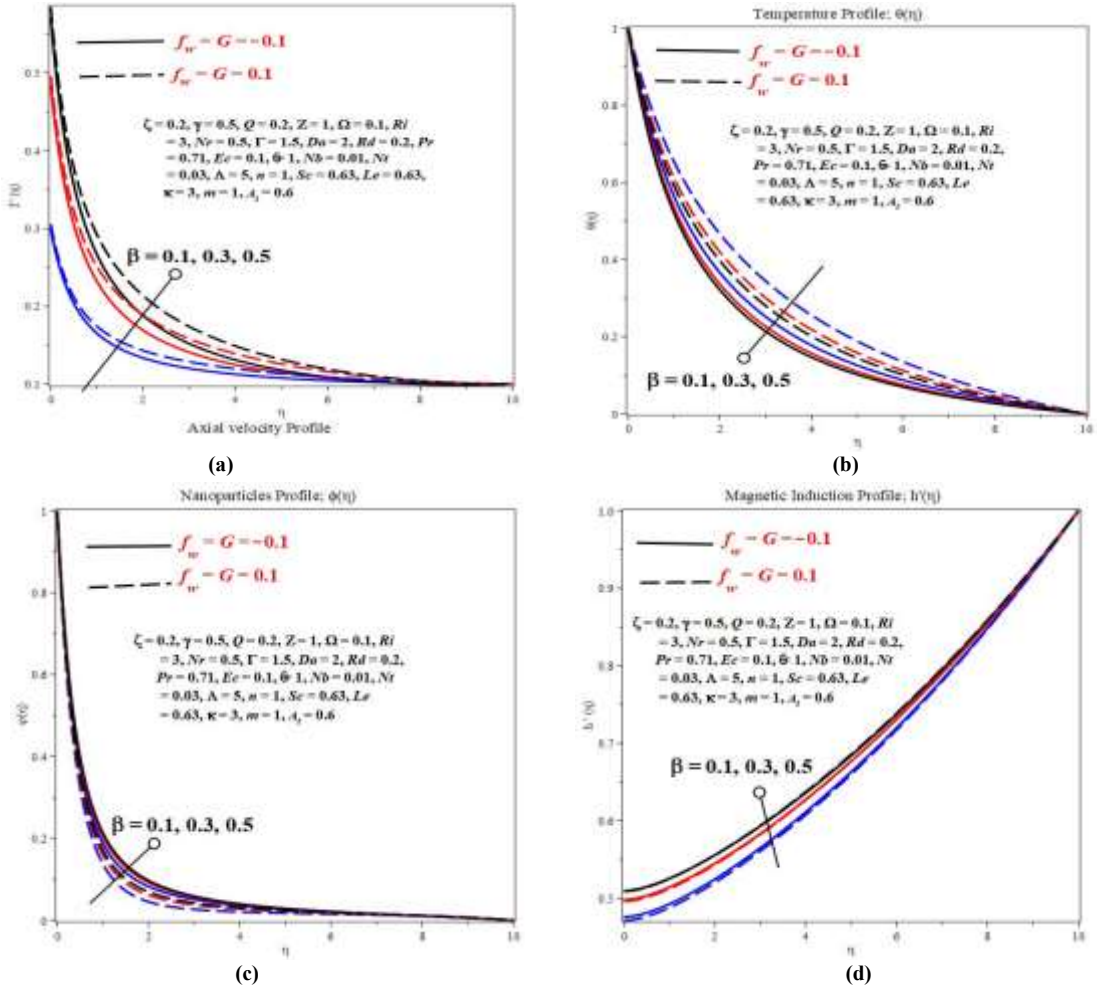

(a) (b)

(c) (d)

Fig. 2 Effect of Casson parameter β on the Flow Fields, Temperature, Nanofluid Flow, and the Magnetic Field Graphs

Slip at the wall moderates shear stress and momentum transfer. Increasing ζ reduces wall adherence, leading to enhanced near-wall velocity (Figure 3a) but lower temperature (Figure 3b) due to reduced viscous dissipation. The magnetic field (Figure 3c) slightly increases near the surface under higher slip because the velocity gradient weakens. Similar thermal attenuation trends occur with β (Figure 2b), showing that both higher β and ζ promoted cooling effects occur in the boundary layer.

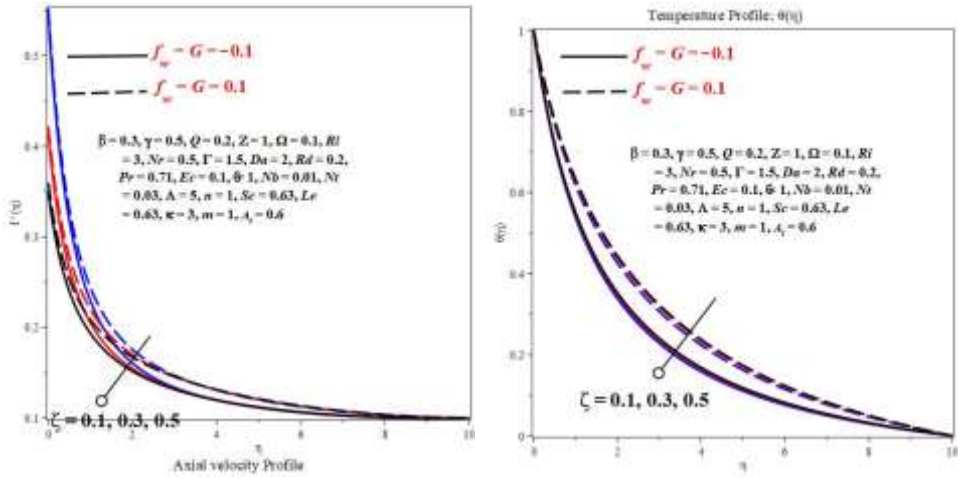

(a) (b)

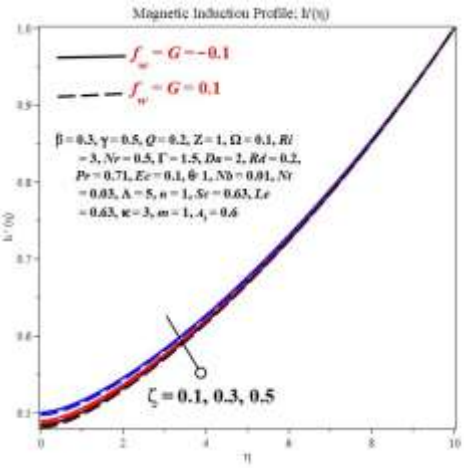

(c)

Fig. 3 Effect of Slip Parameter ζ on the Flow Fields, Temperature, and the Magnetic Field Graphs

The curvature parameter γ modulates the geometrical effects of the cylindrical surface. An increase in γ centrifugal forces strengthens and reduces the radial diffusion layer thickness, enhancing the velocity near the wall (Figure 4a) and also increasing the temperature (Figure 4b). Nanoparticle and magnetic field profiles (Figures 4c & 4d) exhibit similar thinning, indicating stronger convection and better mixing. Comparable cooling effects are observed with higher γ (Figure 2b), showing geometric–hydrodynamic synergy in momentum thermal coupling.

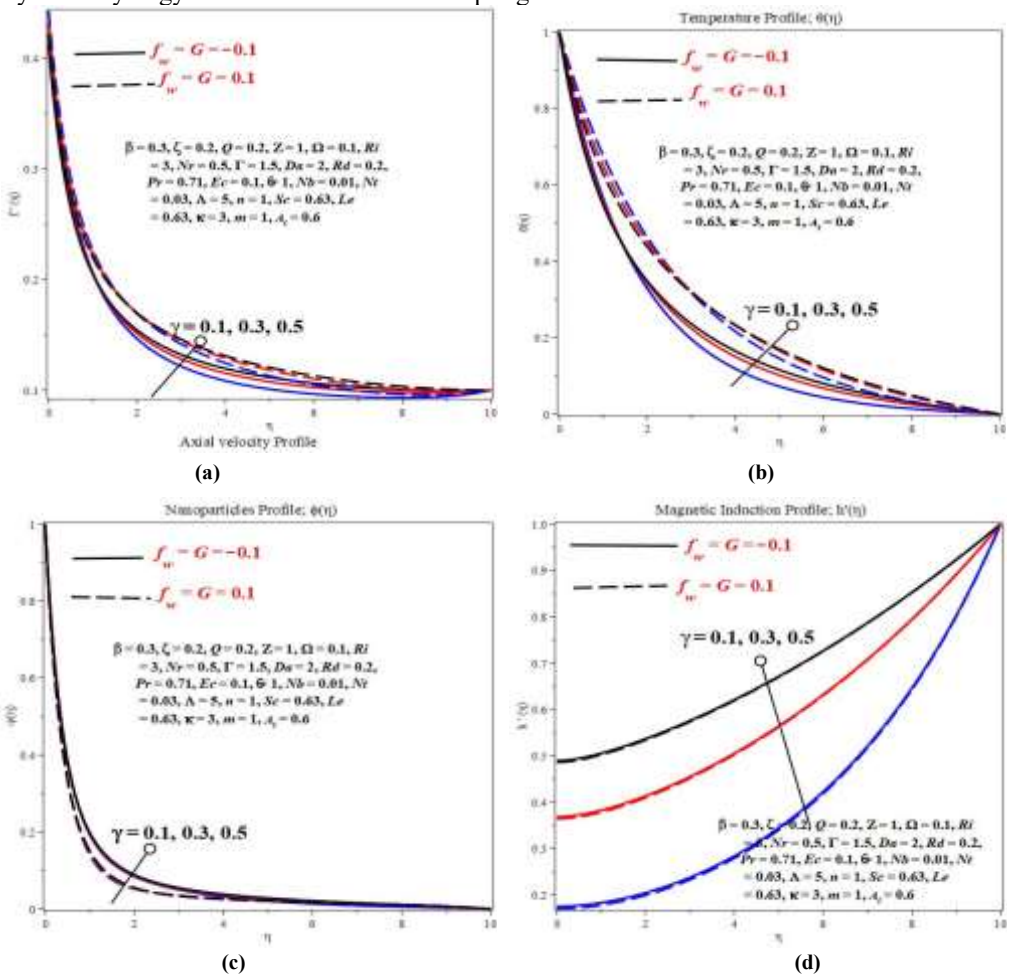

(a) **(b)**

(c) **(d)**

Fig. 4 Effect of Curvature Parameter γ on the Flow Fields, Temperature, Nanofluid Flow, and The Magnetic Field Graphs

RiQuantifies buoyancy relative to inertial forces. Larger values enhance buoyancy-driven flow, thereby increasing velocity (Figure 5a) and slightly lowering temperature (Figure 5b). Nanoparticle concentration (Figure 5c) decreases due to stronger convective transport, while the magnetic field (Figure 5d) becomes more distorted. The behavior parallels β (Figure 2a) and γ (Figure 4a), where increased driving forces raise axial velocity and reduce thermal thickness.

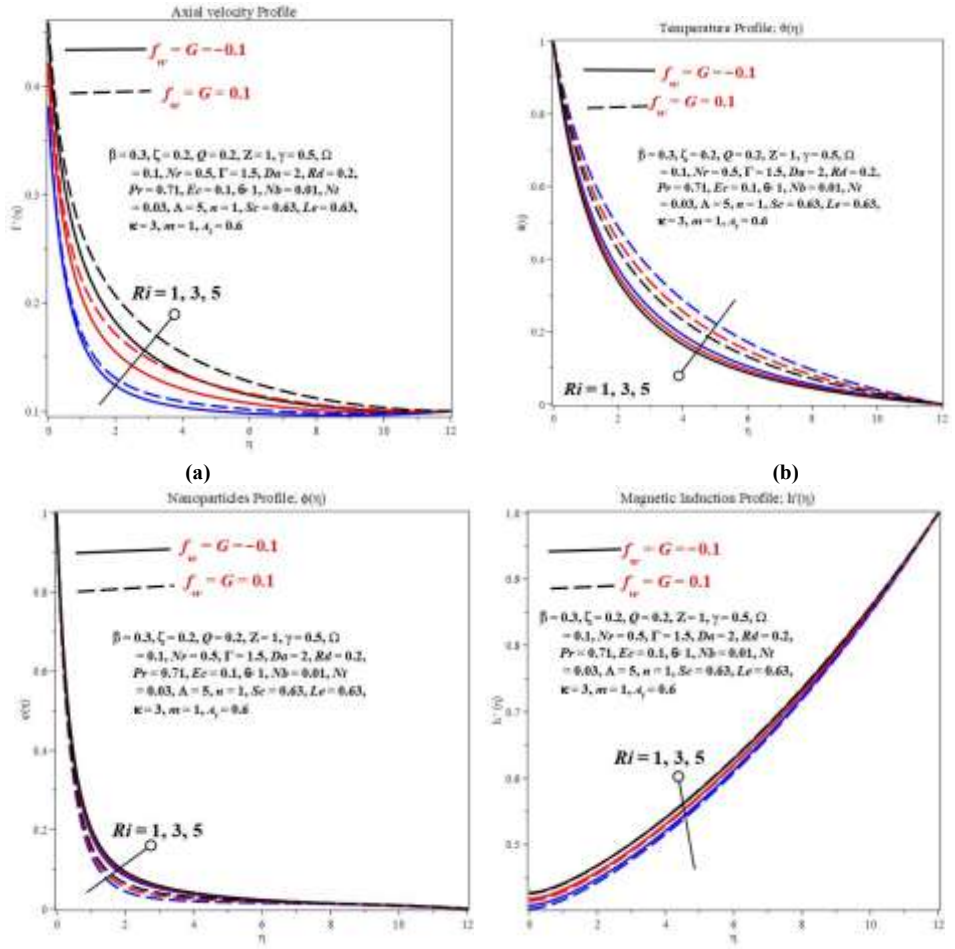

Fig. 5 Effect of Richardson Number on the Flow Field, Temperature, Nanofluid Flow and the Magnetic Field Graphs

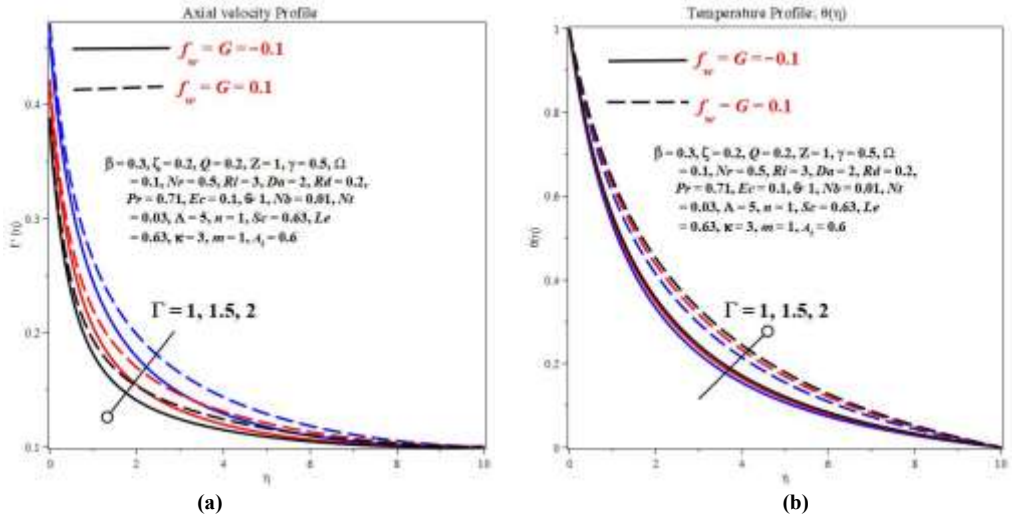

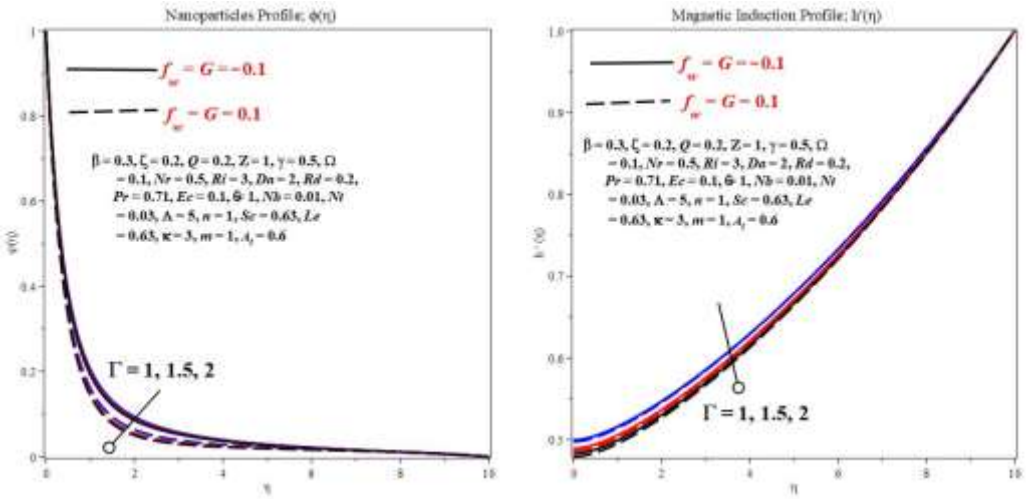

(c) **(d)**

Fig. 6 Effect of Anisotropic Porous Medium Parameter Γ on the flow fields, Temperature, Nanofluid Flow, and the Magnetic Field Graphs

Γcharacterize directional permeability. As the increase, resistance within the porous matrix reduces, leading to an increase in axial velocity (Figure 6a) and cooling of the temperature field (Figure 6b). Nanoparticle and magnetic profiles (Figures 6c & 6d) also thin out, suggesting enhanced filtration and reduced viscous damping. The results mirror the Darcy number effects (Figure 6), indicating that both Γ Da facilitate fluid mobility in porous channels.

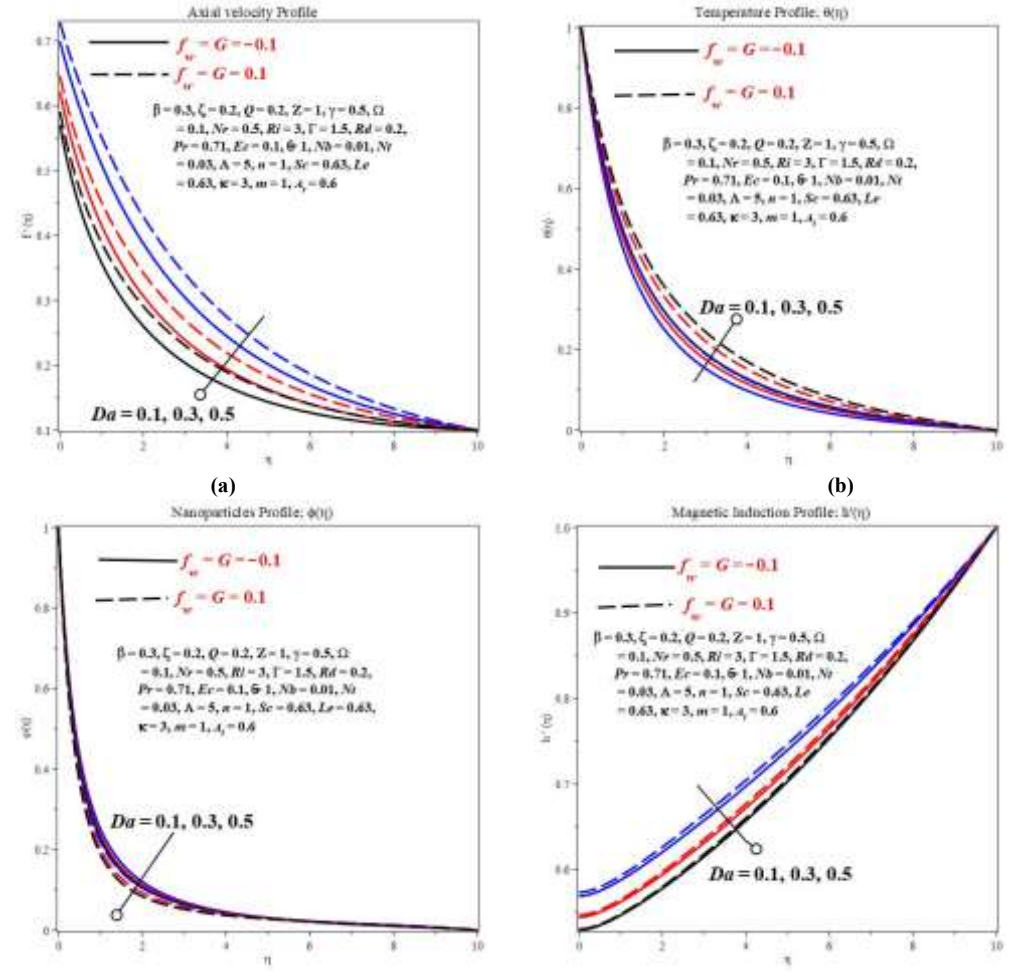

(a) **(b)**

(c) **(d)**

Fig. 7 Effect of Darcy number Da on the Flow field, Temperature, Nanofluid flow, and the Magnetic Field Graphs

Higher Da signifies greater permeability of the porous medium. Increasing Da elevates velocity (Figure 7a) and lowers temperature (Figure 7b) due to improved momentum transport and reduced frictional resistance. Nanoparticle concentration (Figure 7c) also decreases. Similar behavior appears under higher Γ (Figure 5), confirming that permeability (whether isotropic or anisotropic) enhances flow convection.

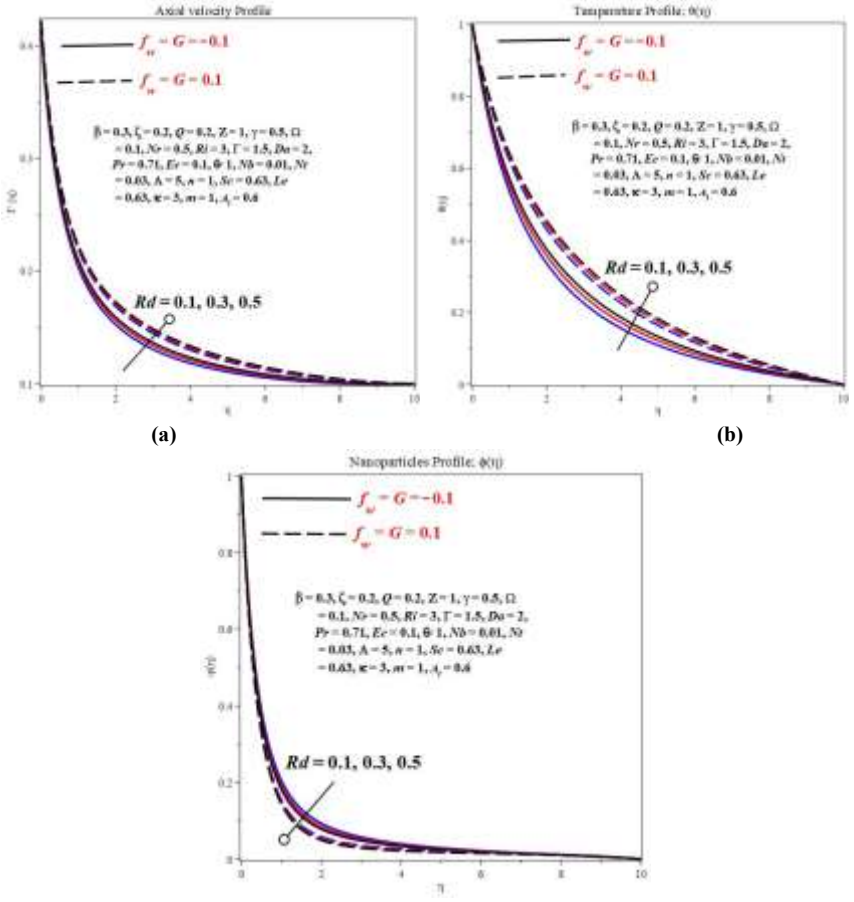

Fig. 8 Effect of Rosseland Radiation Parameter Rd on the Flow Field, Temperature, and Nanofluid Flow Graphs

Radiative heat transfer rises with Rd, augmenting the temperature field (Figure 8b) while slightly reducing velocity (Figure 8a). The nanoparticle layer (Figure 8c) becomes thicker as additional thermal energy enhances Brownian diffusion. The heating trend contrasts with β (Figure 2b) and ς (Figure 3b), where cooling dominates; thus, radiation acts as a competing thermal mechanism.

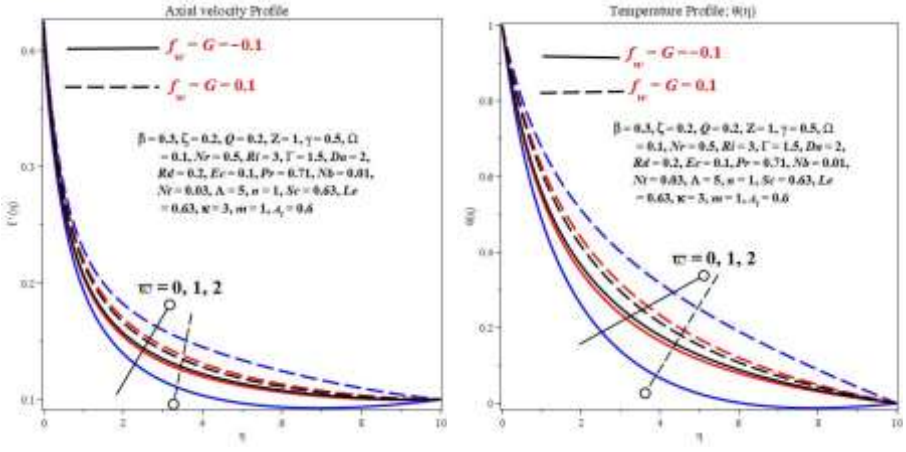

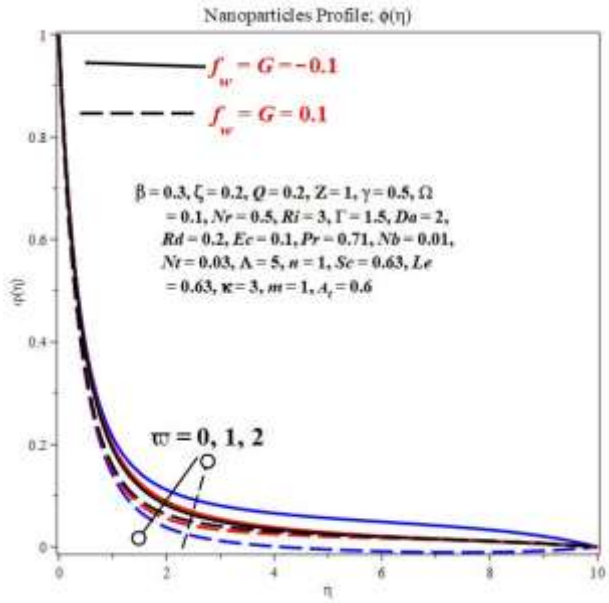

(c)

Fig. 9 Effect of Order of Heat Generation/Absorption G on the Flow Field, Temperature, and Nanofluid Flow Graphs

Increasing the heat generation order $(G > 0)$ elevates temperature (Figure 9b) and reduces velocity (Figure 9a) due to thermal-induced viscosity effects. Conversely, heat absorption $(G < 0)$ cools the system and accelerates flow. Nanoparticle concentration (Figure 9c) follows the same pattern. Similarly, thermal augmentation from Rd (Figure 8b) indicates cumulative heating when both heat source and radiation effects coexist.

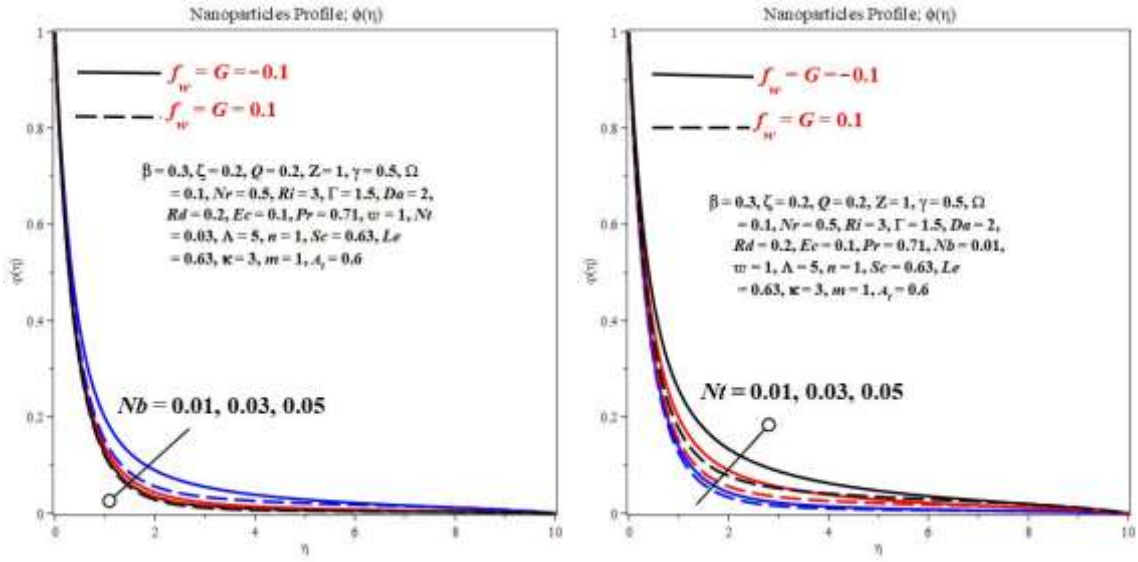

(a) **(b)**

Fig. 10 Effects of Brownian/Thermophoretic (N_b, N_t) Parameters and on the Nanofluid Flow Graphs

Both N_b N_t enhance nanoparticle dispersion. Increased intensity random motion, slightly reducing velocity and elevating temperature, whereas larger N_t induces heat-driven migration, thickening the concentration boundary layer. Together, they improve energy transport but reduce the local Nusselt number. Nanoparticle layer thickening occurs under high Rd conditions G (Figures 7 & 8).

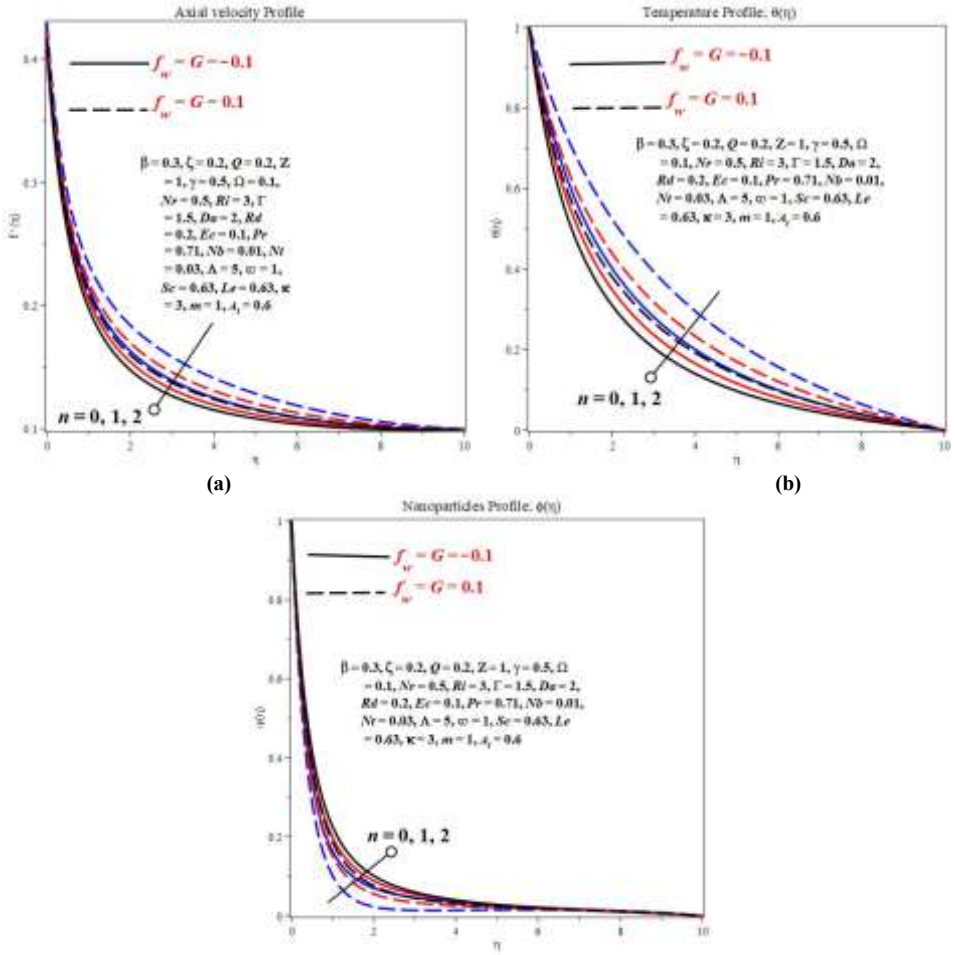

Fig. 11 Effect of Temperature Exponent n on the Flow Field, Temperature, And Nanofluid Flow Graphs

An increase in Λ (Figure 12a) reduces magnetic field intensity by decreasing magnetic diffusivity. Conversely, higher Λ (Figure 12b) intensifies temporal unsteadiness, causing oscillatory fluctuations in the magnetic field. The dynamic trends align with the magnetic suppression seen in β (Figure 2d), indicating that magnetic and rheological properties jointly influence induced field behavior.

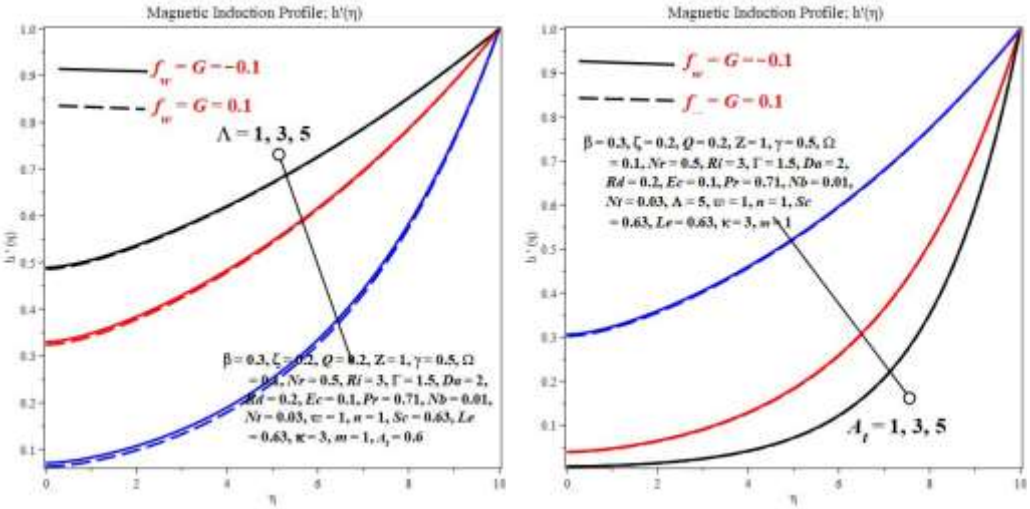

Fig. 12 Effects of Local Inverse Magnetic Prandtl Λ and Local Transient Parameters A_t on Magnetic Field Graphs

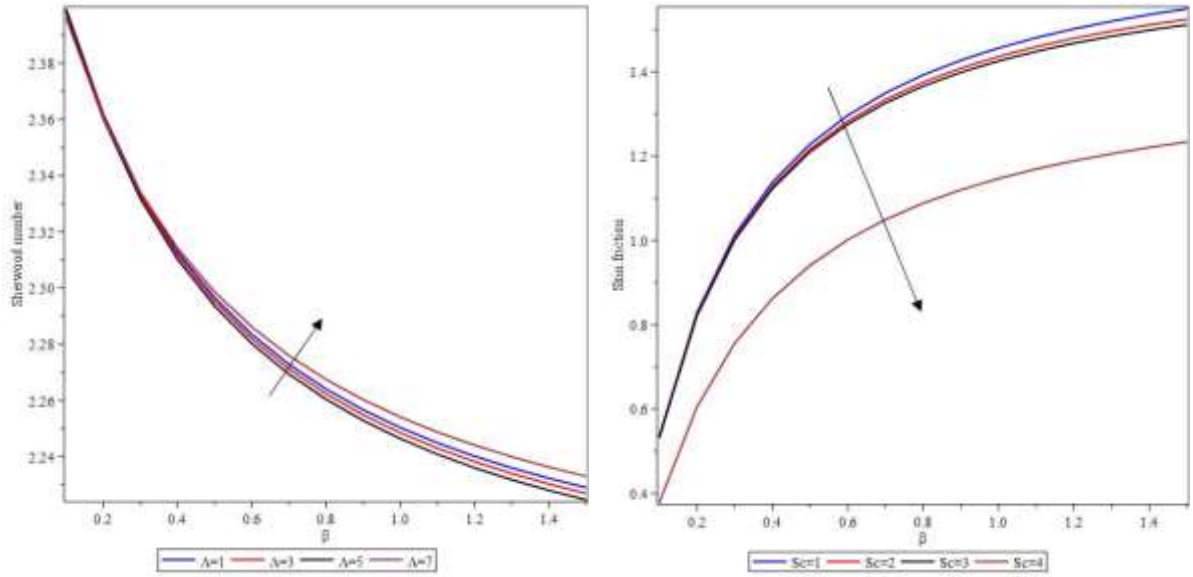

(a) Local Inverse Magnetic Parameter **(b) Schmidt Number**

Fig. 13 Effect of Casson parameter β on Skin-Fiction

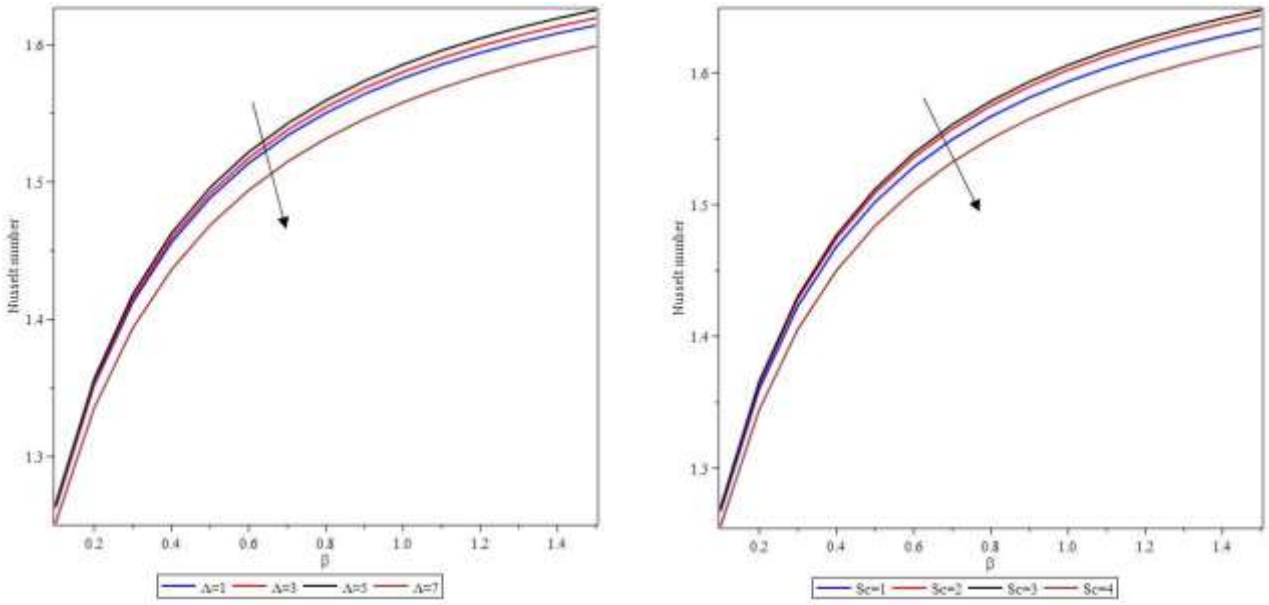

(a) Local Inverse Magnetic Parameter (b) Schmidt Number

Fig. 14 Effect of Casson Parameter β on Nusselt Number

Figures (13–15) illustrate the response of wall shear, heat, and mass transfer coefficients to variations under different Λ Schmidt numbers Sc.

• Skin friction (Figure 13) rises with β and Λ, confirming enhanced near-wall velocity gradients under less viscous conditions.

• Nusselt number (Figure 14) increases with β, showing improved heat transfer for weaker yield stress fluids.

• Sherwood number (Figure 13) exhibits similar trends, emphasizing stronger mass transfer with increasing β Sc.

These results consolidate the earlier field observations (Figures 2–6).

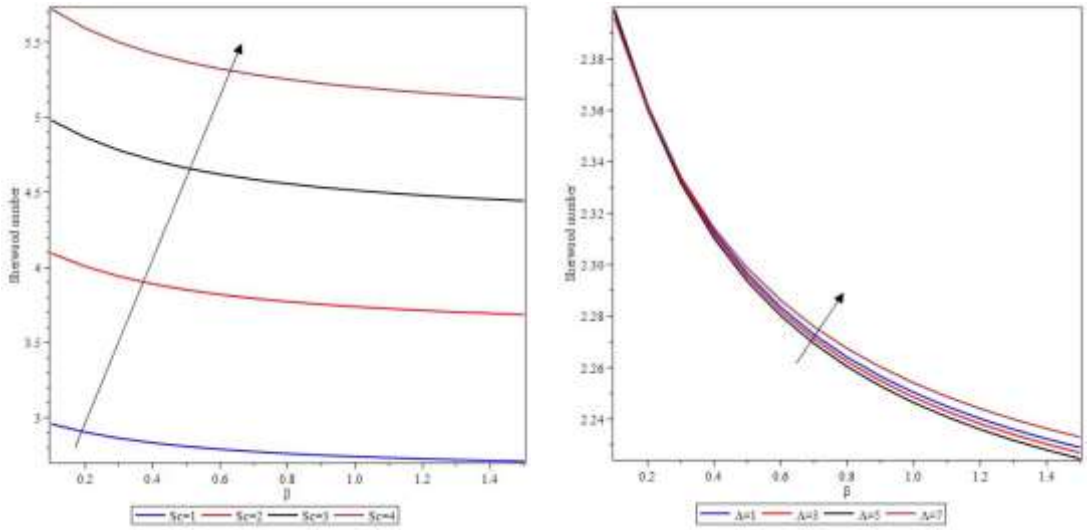

(a) Local Inverse Magnetic Parameter (b) Schmidt Number
Fig. 15 Effect of Casson Parameterβon Sherwood Number

5. Conclusion

5.1. Conclusion

The combined effect of suction/injection$(f_w)$and heat generation/absorption G in a reactive Casson nanofluid over a cylindrical surface within an anisotropic porous medium has been elucidated through the Homotopy Perturbation Method (HPM). The following conclusions are drawn:

- Increasing the Casson parameter β transforms the fluid toward Newtonian behavior, enhancing velocity and reducing temperature.
- Suction strengthens cooling and mass transfer, while injection produces the opposite effect.
- Heat generation and radiation parameters (G, Rd) dominate thermal enhancement but diminish flow intensity.
- Porosity (Γ, Da) and curvature (γ) synergistically boost and slow down convective transport and cooling.
- Magnetic parameters (Q, Λ, A_t) significantly influence field intensity and transient dynamics.

Overall, the interaction between (f_w) and G dictates whether the system acts as a thermal sink or source, offering controllable pathways for industrial thermal fluid optimization.

References

[1] L. Prandtl, "On Fluid Motion Under Very Low Friction," *Proceedings of the 3rd International Mathematical Congress*, Heidelberg, 1904. [Google Scholar]

[2] H. Blasius, *Grenzschichten in Flüssigkeiten Mit Kleiner Reibung*, Druck von BG Teubner, 1907. [Google Scholar] [Publisher Link]

[3] K. Hiemenz, "The Boundary Layer of a Straight Circular Cylinder Immersed in a Uniform Fluid Flow," *Dinglers Polytechnical Journal*, vol. 326, pp. 321-324, 1911. [Google Scholar]

[4] B.C. Sakiadis, "Boundary-layer Behavior on Continuous Solid Surfaces: I. Boundary-layer Equations for Two-dimensional and Axisymmetric Flow," *AIChE Journal*, vol. 7, no. 1, pp. 26-28, 1961. [CrossRef] [Google Scholar] [Publisher Link]

[5] Lawrence J. Crane, "Flow Past a Stretching Plate," *Zeitschrift für angewandte Mathematik und Physik ZAMP*, vol. 21, pp. 645-647, 1970. [CrossRef] [Google Scholar] [Publisher Link]

[6] L.M. Milne-Thomson, *Theoretical Hydrodynamics*, Dover Publications, 1996. [Google Scholar] [Publisher Link]

[7] Michael E. Taylor, *Introduction to Complex Analysis*, American Mathematical Society, 2020. [Google Scholar] [Publisher Link]

[8] Ali J. Chamkha, and Sameh E. Ahmed, "Unsteady MHD Heat and Mass Transfer by Mixed Convection Flow in the Forward Stagnation Region of a Rotating Sphere at Different Wall Conditions," *Chemical Engineering Communications*, vol. 199, no. 1, pp. 122-141, 2012. [CrossRef] [Google Scholar] [Publisher Link]

[9] Donald A. Nield, and Adrian Bejan, *Convection in Porous Media*, Springer, 2006. [Google Scholar]

[10] Izyan Syazana Awaludin, Anuar Ishak, and Loan Pop, "On the Stability of MHD Boundary Layer Flow Over a Stretching/Shrinking Wedge," *Scientific Reports*, 2018. [CrossRef] [Google Scholar] [Publisher Link]

[11] Mohammad Ferdows et al., "Local Non-similar Solution for Non-isothermal Electroconductive Radiative Stretching Boundary Layer Heat Transfer with Aligned Magnetic Field," *Applied Sciences*, vol. 13, no. 7, 2023. [CrossRef] [Google Scholar] [Publisher Link]

[12] K. Stewartson, "The Asymptotic Boundary Layer on a Circular Cylinder in Axial Incompressible Flow," *Quarterly of Applied Mathematics*, vol. 13, no. 2, 1955. [Google Scholar] [Publisher Link]

[13] T. Mahmood, and J.H. Merkin, "Similarity Solutions in Axisymmetric Mixed-convection Boundary- Layer Flow," *Journal of Engineering Mathematics*, vol. 22, pp. 73-92, 1988. [CrossRef] [Google Scholar] [Publisher Link]

[14] R.O. Ayeni, and S.S. Okoya, "On the Skin Friction of an Unsteady Free Convection Flow Past an Oscillating Vertical Porous Plate," *Afrika Matimatika*, vol. 1, no. 2, pp. 101-107, 1988. [Google Scholar]

[15] Chao-Kuang, and Ming I Char, "Heat Transfer of a Continuous, Stretching Surface with Suction or Blowing," *Journal of Mathematical Analysis and Applications*, vol. 135, no. 2, pp. 568-580, 1988. [CrossRef] [Google Scholar] [Publisher Link]

[16] MA Alim, Md M. Alam, and Md MK. Chowdhury, "Pressure Work Effect on Natural Convection Flow from a Vertical Circular Cone with Suction and Non-uniform Surface Temperature," *Journal of Mechanical Engineering*, vol. 36, pp. 6-11, 2008. [CrossRef] [Google Scholar] [Publisher Link]

[17] Henry Darcy, *Les fontaines publiques de la Ville de Dijon*, Victor Dalmont, 1856. [Google Scholar] [Publisher Link]

[18] P. Forchheimer, "Wasserbewegung Durch Boden," *Zeitschrift des Vereines Deutscher Inge- nieure*, vol. 45, pp. 1781-1788, 1901. [Google Scholar] [Publisher Link]

[19] J.H. Merkin, and I. Pop, "Mixed Convection Boundary-layer on a Vertical Cylinder Embedded in a Saturated Porous Medium," *Acta Mechanica*, vol. 66, pp. 251-262, 1987. [CrossRef] [Google Scholar] [Publisher Link]

[20] R.B. Bird, R.C. Armstrong, and O. Hassager, *Dynamics of Polymeric Liquids. Vol. 1: Fluid Mechanics*, U.S. Department of Energy, 1986. [Google Scholar] [Publisher Link]

[21] Stephen U.S. Choi, "Enhancing Thermal Conductivity of Fluids with Nanoparticles," *ASME International Mechanical Engineering Congress and Exposition,* pp. 99-105, 1995. [CrossRef] [Google Scholar] [Publisher Link]

[22] P.A. Davidson, *An Introduction to Magnetohydrodynamics*, Cambridge university Press, 2017. [Google Scholar] [Publisher Link]

[23] J. Buongiorno, "Convective Transport in Nanofluids," *ASME Journal of Heat and Mass Transfer*, vol. 128, no. 3, pp. 240-250, 2006. [CrossRef] [Google Scholar] [Publisher Link]

[24] Mair Khan et al., "Chemically Homann Stagnation Point Flow of Carreau Fluid," *Physica A: Statistical Mechanics and Its Applications*, vol. 551, 2020. [CrossRef] [Google Scholar] [Publisher Link]

[25] H. Alfvén, "Existence of Electromagnetic-Hydrodynamic Waves," *Nature*, vol. 150, pp. 405-406, 1942. [CrossRef] [Google Scholar] [Publisher Link]

[26] A.B. Rosmila, R. Kandasamy, and I. Muhaimin, "Lie Symmetry Group Transformation for MHD Natural Convection Flow of Nanofluid over Linearly Porous Stretching Sheet in Presence of Thermal Stratification," *Applied Mathematics and Mechanics*, vol. 33, pp. 593-604, 2012. [CrossRef] [Google Scholar] [Publisher Link]

[27] P.V.S.N. Murthy et al., "Magnetic Effect on Thermally Stratified Nanofluid Saturated Non-darcy Porous Medium Under Convective Boundary Condition," *International Communications in Heat and Mass Transfer*, vol. 47, pp. 41-48, 2013. [CrossRef] [Google Scholar] [Publisher Link]

[28] P.V. Satya Narayana, "Effects of Variable Permeability and Radiation Absorption on Magnetohy- Drodynamic (MHD) Mixed Convective Flow in a Vertical Wavy Channel with Traveling Thermal Waves," *Propulsion and Power Research*, vol. 4, no. 3, pp. 150-160, 2015. [CrossRef] [Google Scholar] [Publisher Link]

[29] Ali J. Chamkha, Sofen Kumar Jena, and Swarup Kumar Mahapatraa, "MHD Convection of Nanofluids: A Review," *Journal of Nanofluids*, vol. 4, no. 3, pp. 271-292, 2015. [CrossRef] [Google Scholar] [Publisher Link]

[30] N. Casson, "A Flow Equation for Pigment-oil Suspensions of the Printing-ink Type," *Rheology of Disperse System*, pp. 84-104, 1959. [Google Scholar] [Publisher Link]

[31] H.I. Andersson, K.H. Bech, and B.S. Dandapat, "Magnetohydrodynamic Flow of a Power-law Fluid Over a Stretching Sheet," *International Journal of Non-Linear Mechanics*, vol. 27, no. 6, pp. 929-936, 1992. [CrossRef] [Google Scholar] [Publisher Link]

[32] M. Sajid et al., "Unsteady Flow and Heat Transfer of a Second Grade Fluid Over a Stretching Sheet," *Communications in Nonlinear Science and Numerical Simulation*, vol. 14, no. 1, pp. 96-108, 2009. [CrossRef] [Google Scholar] [Publisher Link]

[33] Sohail Nadeem, Rizwan Ul Haq, and Noreen Sher Akbar, "MHD Three-dimensional Boundary Layer Flow of Casson Nanofluid Past a Linearly Stretching Sheet with Convective Boundary Condition," *IEEE Transactions on Nanotechnology*, vol. 13, no. 1, pp. 109-115, 2013. [CrossRef] [Google Scholar] [Publisher Link]

[34] Zahir Shah et al., "Modeling of Entropy Optimization for Hybrid Nanofluid MHD Flow Through a Porous Annulus Involving Variation of Bejan Number," *Scientific Reports*, vol. 10, 2020. [CrossRef] [Google Scholar] [Publisher Link]

[35] M. Tamoor et al., "Magnetohydrodynamic Flow of Casson Fluid Over a Stretching Cylinder," *Results in Physics*, vol. 7, pp. 498-502, 2017. [CrossRef] [Google Scholar] [Publisher Link]

[36] Bhuvaneshvar Kumar, and G.S. Seth, "MHD Stagnation Point Transient Flow of a Nanofluid Past a Stretching Sheet: SRM Approach," *Latin American Applied Research-An International Journal*, vol. 49, no. 3, 2019. [CrossRef] [Google Scholar] [Publisher Link]

[37] I.S. Oyelakin et al., "Bioconvection in Casson Nanofluid Flow with Gyrotactic Microorganisms and Variable Surface Heat Flux," *International Journal of Biomathematics*, vol. 12, no. 4, 2019. [CrossRef] [Google Scholar] [Publisher Link]

[38] Hatem Gasmi et al., "Analysis of Mixed Convection on Two-phase Nanofluid Flow Past a Vertical Plate in Brinkman-extended Darcy Porous Medium with Nield Conditions," *Mathematics*, vol. 10, no. 20, 2022. [CrossRef] [Google Scholar] [Publisher Link]

[39] Raptis, C. Perdikis, and H.S. Takhar, "Effect of Thermal Radiation on MHD Flow," *Applied Mathematics and Computation*, vol. 153, no. 3, pp. 645-649, 2004. [CrossRef] [Publisher Link]

[40] T. Hayat et al., "Magnetohydrodynamic Three-dimensional Flow of Viscoelastic Nanofluid in the Presence of Nonlinear Thermal Radiation," *Journal of Magnetism and Magnetic Materials*, vol. 385, pp. 222-229, 2015. [CrossRef] [Google Scholar] [Publisher Link]

[41] Rekha R. Rangi, and Naseem Ahmad, "Boundary Layer Flow Past a Stretching Cylinder and Heat Transfer with Variable Thermal Conductivity," *Applied Mathematics*, vol. 3, no. 3, 2012. [CrossRef] [Google Scholar] [Publisher Link]

[42] Muhammad Ijaz Khan, and Faris Alzahrani, "Numerical Simulation for the Mixed Convective Flow of Non-newtonian Fluid with Activation Energy and Entropy Generation," *Mathematical Methods in the Applied Sciences*, vol. 44, no. 9, pp. 7766-7777, 2021. [CrossRef] [Google Scholar] [Publisher Link]

[43] M. Monica, J. Sucharitha, and C.H. Kishore, "Effects of Exothermic Chemical Reaction with Arrhenius Activation Energy, Non-uniform Heat Source/Sink on MHD Stagnation Point Flow of a Casson Fluid Over a Nonlinear Stretching Sheet with Variable Fluid Properties and Slip Conditions," *Journal of the Nigerian Mathematical Society*, vol. 36, no. 1, pp. 163-190, 2017. [Google Scholar]

[44] Hazem Ali Attia, "Hiemenz Flow through a Porous Medium of a Non-newtonian Rivlin- Ericksen Fluid with Heat Transfer," *Journal of Applied Science and Engineering*, vol. 12, no. 3, 2009. [CrossRef] [Google Scholar] [Publisher Link]

[45] Adeniyan, F. Mabood, and S.S. Okoya, "Effect of Heat Radiating and Generating Second- grade Mixed Convection Flow Over a Vertical Slender Cylinder with Variable Physical Properties," *International Communications in Heat and Mass Transfer*, vol. 121, 2021. [CrossRef] [Google Scholar] [Publisher Link]

[46] Jihuan He, "Some New Approaches to Dung Equation with Strongly and High Order Nonlinearity (ii) Parametrized Perturbation Technique," *Communications in Nonlinear Science and Numerical Simulation*, vol. 4, no. 1, pp. 81-83, 1999. [CrossRef] [Google Scholar] [Publisher Link]

[47] J.-H. He, "Asymptotology by Homotopy Perturbation Method," *Applied Mathematics and Computation*, vol. 156, no. 3, pp. 591-596, 2004. [CrossRef] [Google Scholar] [Publisher Link]

[48] Ji-Huan He, "A Coupling Method of a Homotopy Technique and A Perturbation Technique for Non-linear Problems," *International Journal of Non-linear Mechanics*, vol. 35, no. 1, pp. 37-43, 2000. [CrossRef] [Google Scholar] [Publisher Link]

[49] Ji-Huan He, "Homotopy Perturbation Method: A New Nonlinear Analytical Technique," *Applied Mathematics and Computation*, vol. 135, no. 1, pp. 73-79, 2003. [CrossRef] [Google Scholar] [Publisher Link]